VOL. 20, NO. 3, FEBRUARY 2025 ISSN 1819-6608
ARPN Journal of Engineering and Applied Sciences

www.arpnjournals.com

DYNAMIC MODELING AND INTEGRAL/FRACTIONAL PID CONTROL FOR A CLASS OF BIOLOGICALLY-INSPIRED CONTINUUM ROBOTS

Amel Djedili, Ammar Amouri and Ayman Belkhiri
Department of Mechanical Engineering, Laboratory of Mechanics, Frères Mentouri Constantine 1 University, Algeria
E-Mail: ameldjedili85@gmail.com

ABSTRACT

This paper presents a simplified nonlinear dynamic model designed specifically for a Dual-Cross-Module Cable-Driven Continuum Robot (DCM-CDCR), which is inspired by a fishbone-like structure. It explores and compares three variants of PID control-the classical Proportional-Integral-Derivative (PID), Optimized PID, and Fractional-Order PID-to mitigate motion oscillations. Unlike CDCRs with cylindrical backbones, the DCM-CDCR offers advantages such as lightweight construction, structural stability, and reduced motor requirements for spatial movement. However, its intricate and highly nonlinear kinematics present challenges in both modeling and control. To tackle these challenges, a forward kinematic model utilizing the Constant Curvature Kinematic Approach (CCKA) is employed to simplify motion representation. The dynamic model, formulated using the Euler-Lagrange formalism, incorporates factors such as gravity, elasticity, and internal moments. The control strategies encompass PID controllers-classical PID, Optimized PID (OPID), and Fractional-Order PID (FOPID). Validation of the proposed models and controllers includes simulation examples that assess static and dynamic responses, along with comparative evaluations of controller performance in target tracking tasks. Furthermore, simulation results are cross-verified with real measurements to validate the static model's accuracy.

Keywords: continuum robot, cable-driven continuum robot, kinematic modeling, dynamic modeling, integral and fractional PID control.

Manuscript Received 19 June 2024; Revised 29 January 2025; Published 21 March 2025

1. INTRODUCTION

Continuum robots have recently attracted considerable attention due to their versatility across various applications [1-3]. Cable-Driven Continuum Robots (CDCRs) represent a notable class in this field, offering configurations with either a single bending section [4, 5] or multiple bending sections connected in series [6, 7]. Each bending section typically comprises a central backbone linking a fixed base to a mobile platform, controlled by cables, where the backbone's role is pivotal in facilitating movement. Consequently, CDCRs have been developed using diverse backbone materials such as elastic/flexible rods [7], springs [5], and plates [8, 9]. The Dual-Cross-Module Cable-Driven Continuum Robot (DCM-CDCR), cited in [8], serves as the focal point of this manuscript.

However, modeling and controlling CDCRs pose significant challenges. The Constant Curvature Kinematic Approach (CCKA) [10] is a prominent kinematic model, with various methods and theories employed, including arc geometry [11], Denavit-Hartenberg method [10], and Cosserat theory [12]. Additionally, researchers have explored numerical and optimization techniques to delve deeper into kinematic modeling [13-15], employing fitting curves like the serpenoid curve [16] and clothoid curves [17] to solve kinematics problems.

Regarding dynamic modeling, numerous methods have been employed to capture the dynamic behavior of CDCRs, including Kane's method [7, 18], Euler-Lagrange formalism [6, 19, 20], and Cosserat rod theory [21, 22].

In terms of controlling CDCRs, the complexity of kinematic and dynamic models presents a challenging yet actively pursued research topic. Researchers have implemented a wide array of control strategies, ranging from classical to advanced ones, including integral and fractional PID control [7, 20, 23], sliding mode control [24], and nonlinear model predictive control [25-26], among others [27-29].

Focusing on the DCM-CDCR [8], this paper contributes by introducing a methodology for dynamic modeling and comparing integral and fractional PID controllers for effective motion control.

The manuscript is structured as follows: Section two offers an overview of the structure and kinematic models of the DCM-CDCR. Section three details the dynamic modeling process, while Section four introduces integral and fractional PID controllers. Section five explores static and dynamic simulation responses, including the stabilization of end-tip-pose controllers, and validates the static model. Finally, the manuscript concludes with a summary in Section six.

2. KINEMATIC MODELING

This section offers a concise overview of the structure and kinematic models of the considered Dual-Cross-Module Cable-Driven Continuum Robot (DCM-CDCR).

2.1 DCM-CDCR Structure

Figure-1 illustrates the structure of the continuum robot, which comprises two identical modules connected

ISSN 1819-6608
ARPN Journal of Engineering and Applied Sciences

in series [8]. Each module consists of three main components: cross-shaped sheets, a sheet-like backbone, and two inextensible cables. More specifically, a spring steel backbone (ASTM A36) measuring $90 \times 26 \times 0.6$ mm forms the foundation of the module. The backbone is accompanied by fifteen cross-shaped sheets made of Z-HIPS polystyrene, each with a diameter of 48 mm and thickness of 3.4 mm. These sheets are evenly distributed and firmly attached to the backbone. Additionally, each cross-shaped sheet includes two holes for the symmetrically distributed driving cables. These cables play a crucial role in controlling the robot's behavior by applying a moment to the tips of the backbones. Importantly, the robot's spatial motion is solely governed by deflection of both backbones simultaneously, enabling a two-Degree-of-Freedom (2-DoF) bending motion.

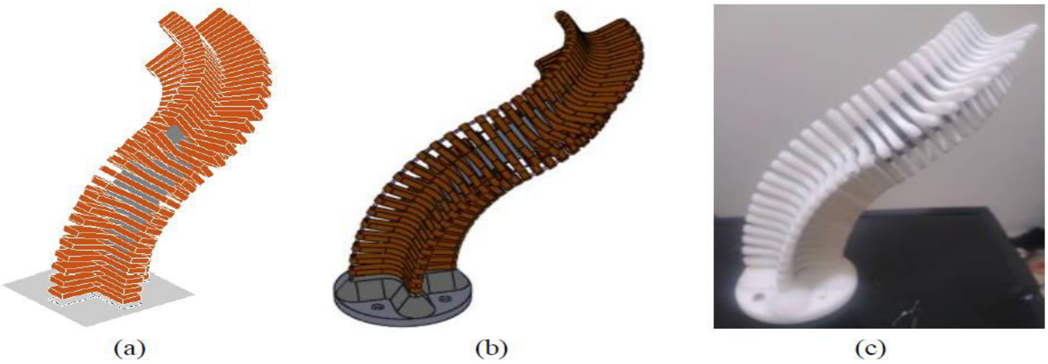

Figure-1. Representation of the DCM-CDCR structure via (a) Matlab software for numerical simulation, (b) Solidworks software for prototyping, and (c) Physical prototype.

2.2 Forward Kinematic Model

The forward kinematic model of the considered DCM-DCR was previously presented in [8]. This model incorporates the Constant Curvature Kinematic Approach (CCKA) and is established on specific assumptions. Based on this model, the vector position $\mathbf{r}_{k,s}$ of any point located on the central axis of the robot's backbones, denoted s, and the rotation matrix $\mathbf{R}_{k,s}$ of any reference frame $\mathcal{R}_{k,s}(o_{k,s}, x_{k,s}, y_{k,s}, z_{k,s})$ relative to the reference frame $\mathcal{R}_0(o_0, x_0, y_0, z_0)$ can be expressed as in Eqs. (1) and (2):

$$\mathbf{r}_{k,s} = \begin{cases} \mathbf{r}_{k,lcl}\,, & k = 1 \\ \mathbf{r}_{k-1} + \mathbf{R}_{k-1}\mathbf{r}_{k,lcl}\,, & k = 2 \end{cases} \tag{1}$$

$$\mathbf{R}_{k,s} = \begin{cases} \mathbf{R}_{k,lcl} = \begin{bmatrix} c\theta_{k,s} & 0 & s\theta_{k,s} \\ 0 & 1 & 0 \\ -s\theta_{k,s} & 0 & c\theta_{k,s} \end{bmatrix}, & k = 1 \\ \mathbf{R}_{k-1}\mathbf{R}_{k,lcl} = \mathbf{R}_{k-1}\begin{bmatrix} 1 & 0 & 0 \\ 0 & c\theta_{k,s} & s\theta_{k,s} \\ 0 & -s\theta_{k,s} & c\theta_{k,s} \end{bmatrix}, & k = 2 \end{cases} \tag{2}$$

such that:

$$\mathbf{r}_{1,lcl} = \left\{ r_1\left(1 - c\theta_{1,s}\right) \;\; 0 \;\; r_1 s\theta_{1,s} \right\}^T \tag{3}$$

$$\mathbf{r}_{2,lcl} = \left\{ 0 \;\; r_2\left(1 - c\theta_{2,s}\right) \;\; r_2 s\theta_{2,s} \right\}^T \tag{4}$$

In these Equations, $\mathbf{R}_k$ denotes the rotation matrix that defines the frame $\mathcal{R}_k(o_k, x_k, y_k, z_k)$ relative to $\mathcal{R}_{k-1}$. The variable r_k, with $k = 1,2$, represents the radius of curvature. This radius can be determined using the formula $r_1 = \ell/\theta_k$, where ℓ and θ_k represent respectively the invariable length and the angle corresponding to the bending of module k. Additionally, $s$refers to the curvilinear abscissa of a module's arc and $\theta_{k,s}$ is the bending angle measured up to s, within the range of $[0, \ell]$, as depicted in Figure-2. The calculation of $\theta_{k,s}$ can be done using the formula $\theta_{k,s} = s\theta_k/\ell$. Lastly, the abbreviations $\mathrm{c}(.)$ and $\mathrm{s}(.)$ represent $\cos(.)$ and $\sin(.)$, respectively.

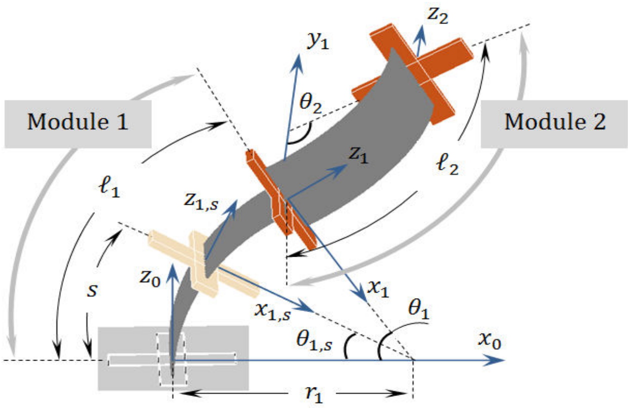

Figure-2. Simplified schematic of the Dual-Cross-Module Cable-Driven Continuum Robot (DCM-CDCR) with defined parameters.

The linear velocity $\dot{\mathbf{r}}_{k,s}$ at any given point located on the central axis of the robot's backbones can be determined by directly differentiating Eq. (1) concerning time, which is demonstrated as in Eq. (5).

ARPN Journal of Engineering and Applied Sciences

On the other hand, the angular velocity $\omega_{k,s}$ can be calculated iteratively according to Eq. (6).

$$\dot{\mathbf{r}}_{k,s} = \begin{cases} \dot{\mathbf{r}}_{k,lcl}, & k = 1 \\ \dot{\mathbf{r}}_{k-1} + \dot{\mathbf{R}}_{k-1}\mathbf{r}_{k,lcl} + \mathbf{R}_{k-1}\dot{\mathbf{r}}_{k,lcl}, & k = 2 \end{cases} \quad (5)$$

$$\omega_{k,s} = \begin{cases} \omega_{k,lcl}, & k = 1 \\ \omega_{k-1} + \mathbf{R}_{k-1}\omega_{k,lcl}, & k = 2 \end{cases} \quad (6)$$

such that:

$$\omega_{k,lcl} = \boldsymbol{t}_{k,lcl} \times \dot{\boldsymbol{t}}_{k,lcl} \quad (7)$$

where $\boldsymbol{t}_{k,lcl}$ represents the third column of the rotation matrix $\mathbf{R}_{k,lcl}$.

However, to develop a dynamic model for the Dual-Cross-Module Cable-Driven Continuum Robot (DCM-CDCR) being studied that is both computationally efficient and accurately captures its main characteristics and that can be used for model-based control, it is crucial to assume mass distribution within the movable part of each module, which includes cross-shaped sheets and a sheet-like backbone. Based on this assumption, the calculation of the position of the center of mass for the movable part of each module, concerning the reference frame $\mathcal{R}_0$ shown in Figure-2, can be determined as in Eq. (8) [30]:

$$\mathbf{r}_{k,G} = \begin{cases} \frac{\int_0^\ell \mathbf{r}_{k,lcl}\mathrm{d}s}{\ell}, & k = 1 \\ \mathbf{r}_{k-1} + \mathbf{R}_{k-1}\frac{\int_0^\ell \mathbf{r}_{k,lcl}\mathrm{d}s}{\ell}, & k = 2 \end{cases} \quad (8)$$

Besides, by directly differentiating the position vector $\mathbf{r}_{k,G}$, it is simple to determine the velocity of the center of mass of each module's movable part. It is noteworthy that Appendix A provides the primary elaborate differential kinematic models required for calculating the dynamic model of the DCM-CDCR.

3. DYNAMIC MODELING

The dynamic model for the DCM-CDCR can be obtained using the Euler-Lagrange formalism along each generalized coordinate θ_k, with $k = 1, 2$, i.e. the bending angle of each module. Formally, the Euler-Lagrange formalism is expressed as in Eq. (9):

$$\frac{d}{dt}\frac{\partial \mathcal{L}}{\partial \dot{\theta}_k} - \frac{\partial \mathcal{L}}{\partial \theta_k} = Q_k \quad (9)$$

where $\mathcal{L} = T - U$ is the Lagrangian that denotes the difference between the kinetic energy $T(\theta_k, \dot{\theta}_k)$ and the potential energy $U(\theta_k)$, and Q_k is the generalized force.

3.1 Kinetic Energy

By utilizing the findings from the previous section, which are specifically elaborated in Appendix A, the total kinetic energy for the DCM-CDCR can be expressed as in Eq. (10):

$$T = \frac{1}{2}\sum_{k=1}^{2} \dot{\mathbf{r}}_{k,G}^T \mathrm{m}_k \dot{\mathbf{r}}_{k,G} + \frac{1}{2}\sum_{k=1}^{2} \omega_{k,mid}^T \boldsymbol{I}_k \omega_{k,mid} \quad (10)$$

where the terms on the right side of Eq. (10) can be interpreted as follows: the first term represents the kinetic energies associated with translational motion, while the second term represents the kinetic energies associated with rotation. m_k is the module's movable part mass. $\omega_{k,mid}$ is the velocity calculated at the middle point of the module k, i.e. at $s = \ell/2$ using Eq. (6). The matrix $\boldsymbol{I}_k$ symbolizes the moment of inertia, which depends on the local moments of inertia I_{xx}, I_{yy} and I_{zz}, as well as the orientation of the movable part of each robot's module. This mathematical relationship can be expressed as in Eq. (11):

$$\boldsymbol{I}_k = \mathbf{R}_{k,mid} \begin{bmatrix} I_{xx} & 0 & 0 \\ 0 & I_{yy} & 0 \\ 0 & 0 & I_{zz} \end{bmatrix} \mathbf{R}_{k,mid}^T \quad (11)$$

where $\mathbf{R}_{k,mid}$ is the rotation matrix calculated at the middle point of the module k, i.e. at $s = \ell/2$ using Eq. (2). I_{xx}, I_{yy} and I_{zz} are the local moments of inertia determined using a static model from CAD.

3.2 Potential Energy

The potential energy of the dual-cross-module cable-driven continuum robot consists of two components. The first component is the gravitational potential energy associated with the masses located at $\mathbf{r}_{k,G}$. The second component is the elastic potential energy of the sheet-like backbones, which depends on the bending angles θ_k of the modules. Therefore, the total potential energy can be expressed as in Eq. (12):

$$U = \sum_{k=1}^{2} \mathrm{m}_k \mathbf{g}^T \mathbf{r}_{k,G} + \sum_{k=1}^{2} \frac{EI_b}{2\ell}\theta_k^2 \quad (12)$$

where $\mathbf{g} = [0, 0, -\mathrm{g}]^T$ is the gravity vector, E is the modulus of elasticity and I_b is the second moment of the cross-sectional area of each elastic sheet-like backbone.

3.3 Generalized Forces

In fact, a generalized force Q_k represents the combined effect of all forces acting on the selected generalized coordinate θ_k. These forces encompass actuation forces, friction forces, and any external loads. However, the examined robot stated in [8] has a significant limitation in that it cannot support any

ISSN 1819-6608
ARPN Journal of Engineering and Applied Sciences

additional weight. Therefore, this study focused solely on the robot's weight and did not consider any external loads. To simplify the analysis, the frictional forces were ignored, and the internal moment at each module was considered as the structural frictional moment. Moreover, the actuation system is approximately modeled by the tip moment at each robot's module. As a result, the equation representing the total force affecting each module of the robot can be expressed as in Eq. (13):

$$U = \frac{d}{2}\left(F_{k,1} - F_{k,2}\right) - C_{fr} \sum_{i=1}^{k} \dot{\theta}_i^2 \tag{13}$$

where the terms on the right side of Eq. (13) can be interpreted as follows: the first term corresponds to a simplified model of the force applied to bend the robot's module k. To provide a clearer explanation of this mathematical statement, if $F_{k,1}$ is greater in magnitude than $F_{k,2}$, then it suggests that the unit's rotation or bending movement is in a clockwise direction. Conversely, if $F_{k,2}$ is greater in magnitude than $F_{k,1}$, then the movement occurs in the opposite direction. d represents the distance between the driving cables. To illustrate the variation in cable tensions, Figure-3 exhibits a scheme illustrating how the tensions in the four cables change for the two modules, ensuring the intended motion of the robot. The second term in the equation signifies the internal moments experienced by each module [30, 31], with C_{fr} representing the friction coefficient. In this study, for the sake of simplicity, the friction effect is neglected.

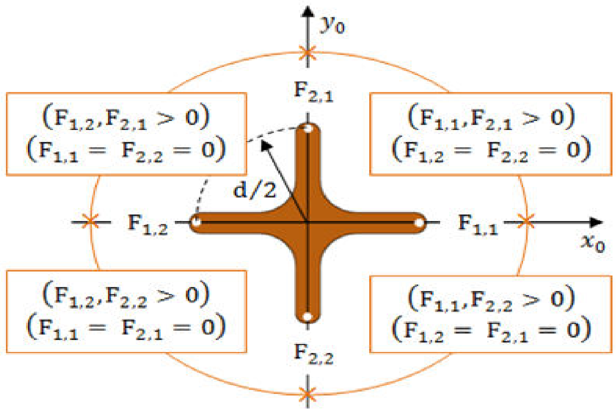

Figure-3. An illustrative scheme, taken from the top view of the studied robot, providing a visual representation of how the tension in the cables changes in order to carry out any motion of the robot.

3.4 Resulting Dynamic Model

By substituting the derivatives of the Lagrangian $\mathcal{L}$ and generalized forces Q_k into Eq. (9) for the selected generalized coordinate θ_k, and subsequently developing the expressions, two coupled second-order differential equations are obtained representing the motion equations for the dual-cross-module cable-driven continuum robot, presented in the general form as in Eq. (14):

$$\mathbf{M}(\mathbf{q})\ddot{\mathbf{q}} + \mathbf{C}(\mathbf{q}, \dot{\mathbf{q}})\dot{\mathbf{q}} + \mathbf{K}(\mathbf{q}) = \mathbf{Q} \tag{14}$$

where the inertia matrix $\mathbf{M}(\mathbf{q}) \in \mathbb{R}^{(2\times2)}$, centripetal-Coriolis terms $\mathbf{C}(\mathbf{q}, \dot{\mathbf{q}}) \in \mathbb{R}^{(2\times3)}$, gravitational vector $\mathbf{K}(\mathbf{q}) \in \mathbb{R}^{2}$ are provided in Appendix B. The vector $\mathbf{q} \in \mathbb{R}^{2}$ represents the generalized coordinates, while $\mathbf{Q} \in \mathbb{R}^{2}$ is the input force vector.

To simulate and analyze how the robot responds to different inputs and outputs, it is necessary to express the dynamics equations obtained in Eq. (14) in the following manner as in Eq. (15):

$$\dot{\mathbf{S}}(t) = f(\mathbf{S}, t) + h(\mathbf{S}, t)\mathbf{u}(t) \tag{15}$$

where $f(.)$ and $h(.)$ are nonlinear functions, urepresents the command vector, t is the time parameter, and $\mathbf{S}$ represents the state variable vector, which is given as in Eq. (16):

$$\mathbf{S}(t) = \begin{cases} S_1 = \theta_1(t) \\ S_2 = \dot{\theta}_1(t) \\ S_3 = \theta_2(t) \\ S_4 = \dot{\theta}_2(t) \end{cases} \tag{16}$$

4. CONTROL SYSTEM DESIGN

It is evident from Eq. (14) that the dynamic model of the Dual-Cross-Module Cable-Driven Continuum Robot (DCM-CDCR) constitutes a complex and nonlinear system. In this section, the aim is to manage this robotic system by implementing three control strategies, namely the classical Proportional-Integral-Derivative (PID) controller, the Optimized PID controller (OPID), and the Fractional-Order Proportional-Integral-Derivative (FOPID) controller.

The FOPID controller, which was first introduced by Podlubny in 1999 [32], represents an extension of the classical PID controller by incorporating fractional calculus principles. This novel development has allowed for enhanced control capabilities and improved performance in various applications. By integrating fractional calculus techniques, the FOPID controller introduces additional degrees of freedom and flexibility, enabling it to effectively handle complex control tasks.

The FOPID controller symbolized as $PI^{\lambda}D^{\mu}$, includes the PID and OPID controllers as a specific instance where $\lambda = \mu = 1$. Figure-4 provides an overview of the connection between the classical PID controller and the FOPID controller, highlighting the

VOL. 20, NO. 3, FEBRUARY 2025 ISSN 1819-6608
ARPN Journal of Engineering and Applied Sciences

www.arpnjournals.com

influence of the λ and μ parameters. In simpler terms, the PID and OPID controllers fall under the category of FOPID controllers, and their relationship is illustrated in Figure-4 based on the values assigned to λ and μ. It is important to highlight that the FOPID controller enhances the performance and robustness of the controlled system through the parameters λ and μ. However, tuning the parameters of this controller can be challenging due to the complex behavior exhibited by many robotic systems, including the robot under consideration. To effectively tackle this problem, we propose the utilization of a Particle Swarm Optimization (PSO) algorithm [33]. This algorithm not only tunes the parameters of the FOPID controller but also optimizes the parameters of the OPID controller. The parameters of the classical PID controller, on the other hand, are determined through a trial-and-error method.

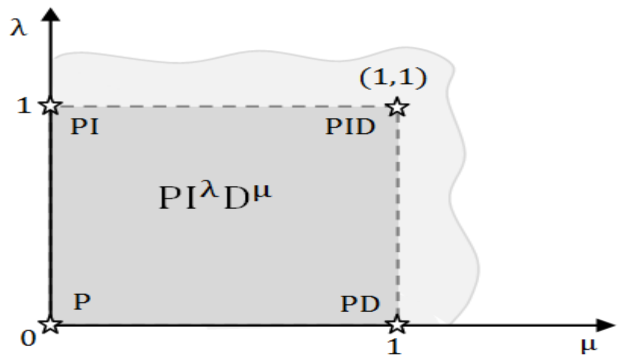

Figure-4. Relationships among integral and fractional PID variants.

Since the robot under consideration has 2-DoF, specifically two generalized coordinates θ_1 and θ_2, it is necessary to implement two discrete controllers. These controllers can be PID, OPID, or FOPID controllers. One controller is used to regulate the bending angle θ_1 of the first module, while the other controller controls the bending angle θ_2 of the second module. However, because the two modules of the robot possess identical geometrical and inertial characteristics and properties, it is preferable to choose similar parameters for both controllers. Consequently, the control law $\mathrm{u}_k(t)$, with $k = 1{,}2$, is defined as in Eq. (17):

$$\mathrm{u}_k(t) = K_P e_{\theta_k}(t) + K_I D^{-\lambda} e_{\theta_k}(t) + K_D D^{\mu} e_{\theta_k}(t) \qquad (17)$$

where K_P, K_I, and K_D represent the proportional, integral, and derivative coefficients in the given context. λ and μ represent the integral and derivative orders respectively. $D(.)$ denotes the generalized integration and differentiation operator, which is a frequently used operation in fractional calculus. When both λ and μ are equal to 1, the controller becomes a PID controller. The objective of all controllers is to minimize the tracking error $e_{\theta_k}(t)$, which is defined as the difference between the desired position of the DCM-CDCR's end-tip, denoted by $\theta_{k,\mathrm{d}}(t)$, and the generated position, denoted by $\theta_{k,\mathrm{g}}$.

5. NUMERICAL SIMULATION AND EXPERIMENTAL VALIDATION

To confirm the validity of the dynamic model developed, a numerical simulation was conducted using MATLAB software. The simulation utilized the Runge-Kutta method as a numerical solution to assess the dynamic behavior of the Dual-Cross-Module Cable-Driven continuum Robot (DCM-CDCR). The parameters for the simulated robot are provided in Table-1. Two different cases were analyzed: static response and dynamic response. Furthermore, a static modal experiment was conducted to validate the proposed dynamic model's efficiency in terms of accuracy. Additionally, a simulation example was carried out to evaluate the effectiveness and control performance of the proposed controllers, namely: PID controller, OPID controller, and FOPID controller, in set-point tracking tasks. The optimal parameters for the three controllers have been included in Table-2.

Table-1. Parameters for the simulated robot.

Para.	Designation	Value
d	Distance between the driving cables	46 mm
E	Elasticity modulus	$2 \cdot 10^{11}$ N/m^2
g	Gravity constant	9.81 N/s^2
I_b	Inertia moment of the backbone	$817.97 \cdot 10^{-3}$ Kg/mm^2
I_x	Local inertia moment along x −axis of the cross-shaped sheet	$175.70 \cdot 10^{-3}$ Kg/mm^2
I_y	Local inertia moment along y −axis of the cross-shaped sheet	$173.13 \cdot 10^{-3}$ Kg/mm^2
ℓ	Module length	90 mm
m	Backbone mass	$26.21 \cdot 10^{-3}$Kg

Table-2. Optimal parameters of controllers.

Parameters	PID	OPID	FOPID
K_P	6.186	1.0964	2.1635
K_D	1.175	5.7056	5.2320
K_I	3.725	0.7885	11.2252
λ	1	1	0.778
μ	1	1	0.712

VOL. 20, NO. 3, FEBRUARY 2025 ISSN 1819-6608
ARPN Journal of Engineering and Applied Sciences

5.1 Static Response

The robot's static response involves analyzing the dynamic behavior of the robot in a state when the input tensions of the driving cables are all zero. This analysis is based on assumed initial bending angle conditions. Two cases are considered, one with initial angles set as $\theta_1 = \pi/4$ and $\theta_2 = 0$, and the other with angles set as $\theta_1 = 0$ and $\theta_2 = \pi/4$. It should be noted that when the bending angles reach zero, certain expressions in the dynamic model become indeterminate. To address this issue, we substitute asymptotic values close to zero for these singularities.

The first oscillations of the DCM-CDCR after release for both cases are shown in Figures 5 and 6, respectively. From the analysis of these Figures, although the transverse arrangement of the backbones' modules, the module initialized with a value of the bending angle experiences also minor oscillations. These oscillations occur due to assigning a small value $(\theta_1 = \theta_2 = 0.002 \text{ rad})$ to avoid numerical singularities, as estimated during this study.

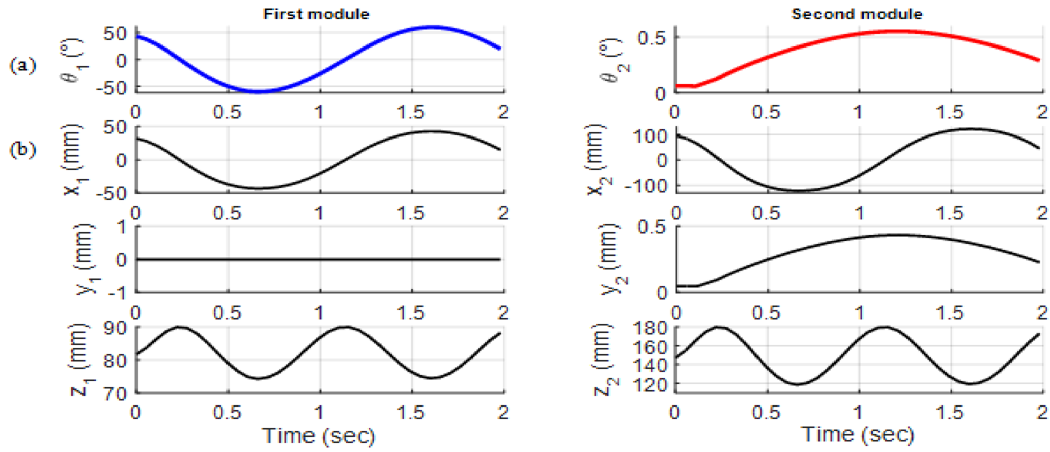

Figure-5. Static responses of the robot dynamic model with zero actuation under initial conditions $\theta_1 = \pi/4$ and $\theta_2 = 0$: (a) response of the bending angles, (b) end-tip displacements of each module of the DCM-CDCR.

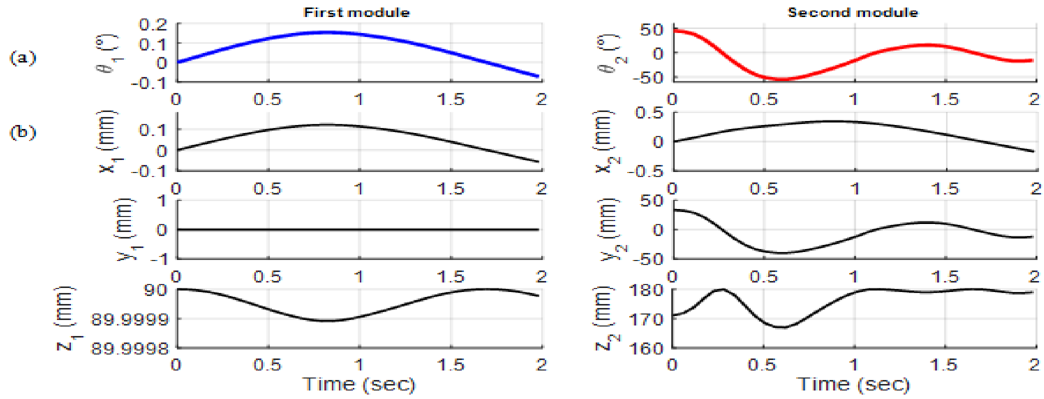

Figure-6. Static responses of the robot dynamic model with zero actuation under initial conditions $\theta_1 = 0$and $\theta_2 = \pi/4$: (a) response of the bending angles, (b) end-tip displacements of each module of the DCM-CDCR.

5.2 Dynamic Response

This subsection explores two simulation examples to illustrate the dynamic responses of the DCM-CDCR under consideration. The first example emphasizes target tracking, while the second addresses trajectory tracking using a point-to-point approach.

For the first example, three scenarios are investigated: applying a step input of 2 N as tension in cables (1,1), (2,1), and both cables (1,1) and (2,1) simultaneously (refer to Figure-2). These simulations initiate from the vertical initial posture of the robot's equilibrium. Figure-7 illustrates the dynamic responses of the bending angles for the three analyzed cases.

VOL. 20, NO. 3, FEBRUARY 2025 ISSN 1819-6608
ARPN Journal of Engineering and Applied Sciences

www.arpnjournals.com

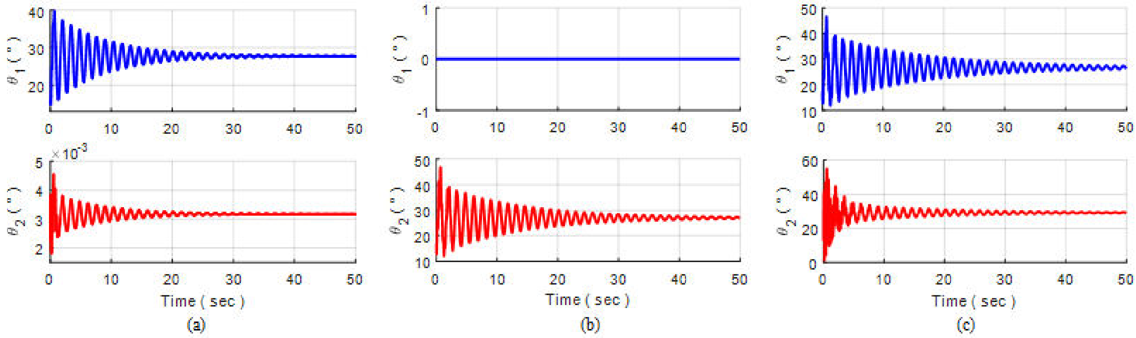

Figure-7. Dynamic responses of the DCM-CDCR for a step input of 2 N: (a) actuation of the first robot's module, (b) actuation of the second robot's module, and (c) actuation of both robots' modules simultaneously.

In the second example, the dynamic model takes the spatial trajectory depicted in Figure-8 as input. The dynamic responses, including the bending angles and required tension forces in cables, are presented in Figures 9 and 10, respectively. Additionally, utilizing the kinematic models, Figure-11 showcases the temporal evolution of the cable lengths of the DCM-CDCR as it tracks the desired spatial trajectory.

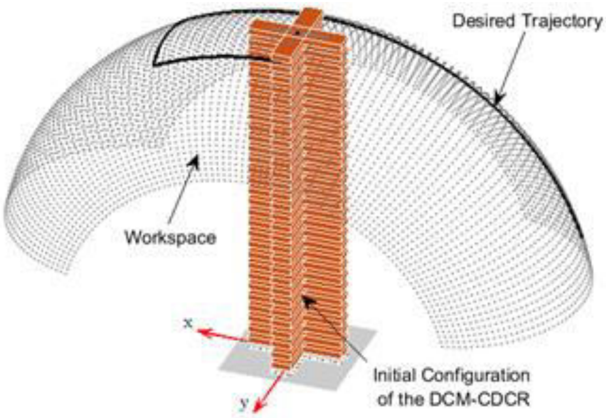

Figure-8. Visualization of the complex trajectory to be tracked within the DCM-CDCR workspace.

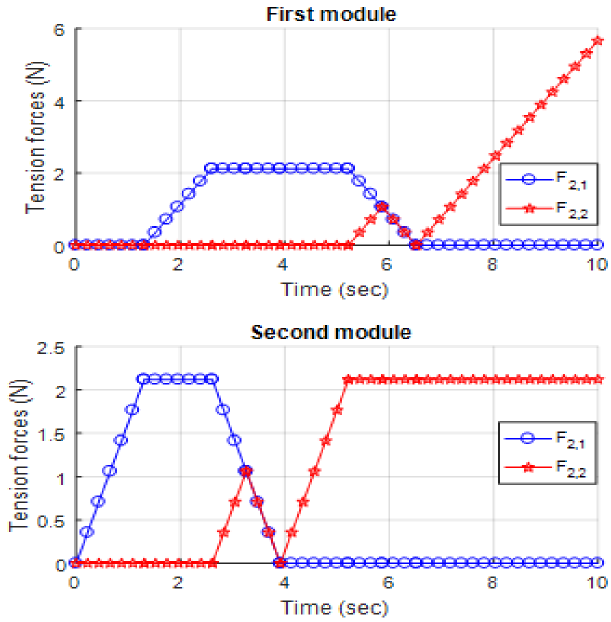

Figure-9. Temporal evaluation of tension forces required to track the desired complex trajectory.

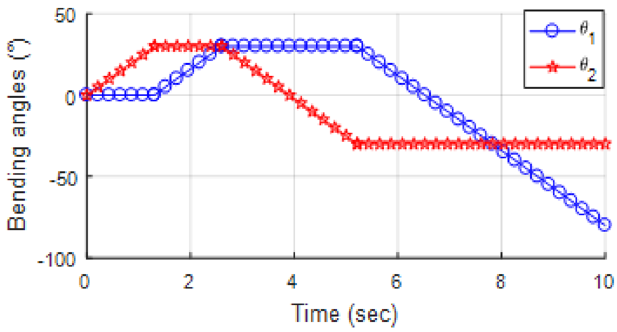

Figure-10. Temporal evaluation of bending angles required to track the desired complex trajectory.

VOL. 20, NO. 3, FEBRUARY 2025 ISSN 1819-6608
ARPN Journal of Engineering and Applied Sciences

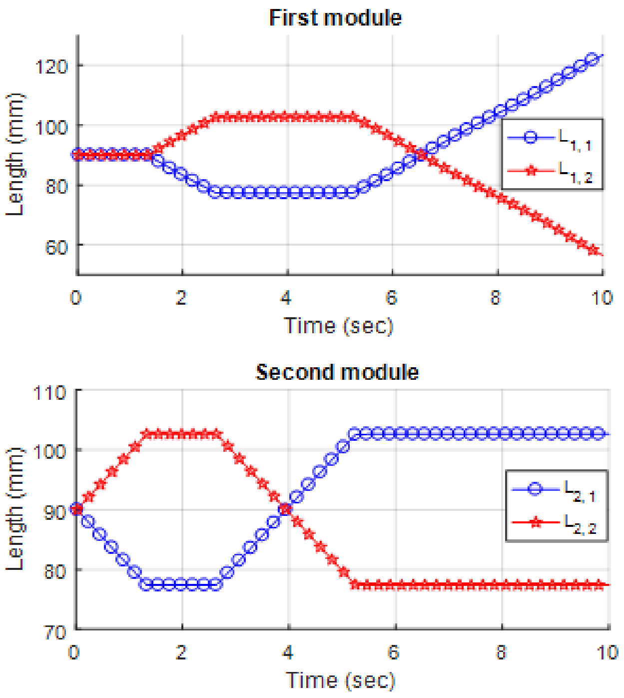

Figure-11. Temporal evaluation of cable lengths required to track the desired complex trajectory.

5.3 Static Model Validation

To assess the accuracy and efficiency of the static model, this subsection compares its results, obtained from the dynamic model of the DCM-CDCR, with real measurements. To accomplish this, two scenarios are examined: the first scenario involves activating only the first module of the DCM-CDCR, while the second scenario involves activating only the second module.

Figure-12 illustrates the experimental setup used to determine the Cartesian position of the DCM-CDCR's end-tip in response to the tension force applied to a cable. The setup comprises: (i) a physical prototype, (ii) a portable 3D measuring arm (Romer Absolute Arm, Model RA-7312) serving as an external Cartesian position sensor to monitor the DCM-CDCR end-tip relative to its reference frame, and (iii) a manual cable actuation device for maneuvering the DCM-CDCR.

The comparison results for the two scenarios are depicted in Figures 13 and 14, respectively. Analysis of these Figures reveals a significant alignment between the simulation and measurement outcomes. Nevertheless, minor discrepancies are evident, possibly stemming from various factors, including the influence of gravity on the DCM-CDCR components, which were overlooked in the simulation, potential inaccuracies in the measurements, as well as the modeling assumptions and approximations mentioned earlier.

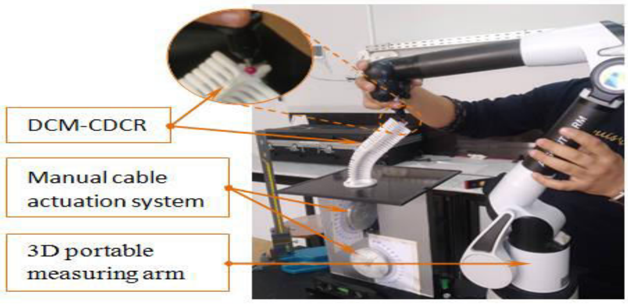

Figure-12. Test bench overview.

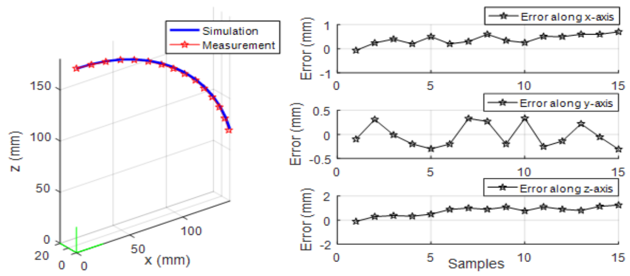

Figure-13. Comparative analysis of measured and calculated Cartesian positions of DCM-CDCR end-tip for the first scenario, with only the first module of DCM-CDCR operational.

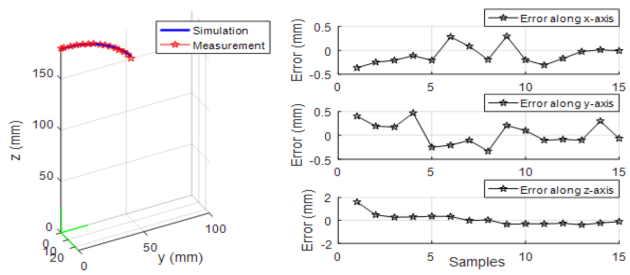

Figure-14. Comparative analysis of measured and calculated Cartesian positions of DCM-CDCR end-tip for the second scenario, with only the second module of DCM-CDCR operational.

5.4 Implementation of PID Controllers

To mitigate oscillations around the newly established stable value of the bending angles, as depicted in Figure-7, and to efficiently control the robot, three variants of PID controllers-PID, OPID, and FOPID-are employed. These controllers are evaluated based on their performance in set-point tracking tasks. Figure-15 presents a comparative analysis of tracking performance among the three controllers across the scenarios outlined in Subsection 5.2. It is evident from Figure-15 that the FOPID controller, followed by the OPID, offers better control performance compared to the classical PID controller. This difference can be attributed to the influence of the two additional parameters of the FOPID Controller, the fractional integral order λ, and the derivative μ.

VOL. 20, NO. 3, FEBRUARY 2025 ISSN 1819-6608
ARPN Journal of Engineering and Applied Sciences

www.arpnjournals.com

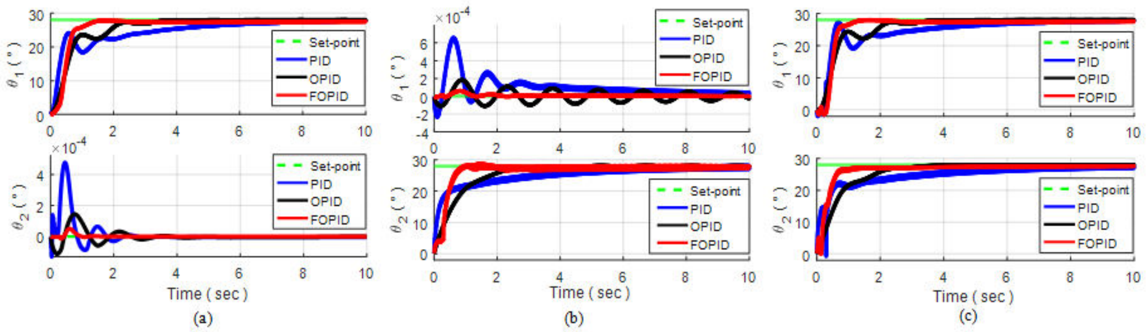

Figure-14. Comparative analysis of dynamic responses of the DCM-CDCR to a 2 N step input with three PID controllers and their corresponding tension forces:(a) activation of the first robot module, (b) activation of the second robot module, and (c) simultaneous activation of both robot modules.

6. CONCLUSIONS

In this paper, a simplified nonlinear dynamic model is presented for a category of continuum robots known as Dual-Cross-Module Cable-Driven Continuum Robots (DCM-CDCR). Initially, the forward kinematic model is formulated using the Constant Curvature Kinematic Approach (CCKA) due to its simplification in modeling. Subsequently, the dynamic model is developed using the Euler-Lagrange formalism, taking into account factors such as gravity, elasticity, and internal moments. The validity of the modeling approach is confirmed through various simulation examples covering static, in-plane actuation, out-of-plane actuation, and dynamic scenarios.

Additionally, real measurements are conducted to verify the accuracy of the static model. Finally, to address oscillations in the dynamic responses, three PID control variants are implemented and assessed based on their performance in set-point tracking tasks.

Looking ahead, building upon the foundation of the 2-DoF module, we aim to expand the developed dynamic model to accommodate multiple-DoF continuum robots. Additionally, we plan to incorporate factors such as torsion, friction, and all gravitational effects to better approximate the real behavior of the robot.

Appendix A: Derived differential kinematic models

$$\dot{\mathbf{r}}_{1,G}=\begin{cases}-\dfrac{\ell\dot{\theta}_1(\theta_1-2s\theta_1+\theta_1 c\theta_1)}{\theta_1^3},\\ 0,\\ \ell\dot{\theta}_1\left(\dfrac{s\theta_1}{\theta_1^2}+\dfrac{2(c\theta_1-1)}{\theta_1^3}\right),\end{cases}$$

$$\dot{\mathbf{r}}_{2,G}=\begin{cases}\ell\dot{\theta}_1\left(\dfrac{s\theta_1}{\theta_1}+\dfrac{2(c\theta_1-1)}{\theta_1^2}-\dfrac{c\theta_1(c\theta_2-1)}{\theta_2^2}\right)+\ell\dot{\theta}_2\left(+\dfrac{2s\theta_1(c\theta_2-1)}{\theta_2^3}+\dfrac{s\theta_1 s\theta_2}{\theta_2^2}\right),\\ \ell\dot{\theta}_2\left(+\dfrac{-2(\theta_2-s\theta_2)}{\theta_2^3}-\dfrac{(c\theta_2-1)}{\theta_2^2}\right),\\ \ell\dot{\theta}_1\left(\dfrac{c\theta_1}{\theta_1}-\dfrac{s\theta_1}{\theta_1^2}+\dfrac{s\theta_1(c\theta_2-1)}{\theta_2^2}\right)+\ell\dot{\theta}_2\left(+\dfrac{2c\theta_1(c\theta_2-1)}{\theta_2^3}+\dfrac{c\theta_1 s\theta_2}{\theta_2^2}\right),\end{cases}$$

ARPN Journal of Engineering and Applied Sciences

Appendix B: Components of matrices utilized in Eq. (14)

$$\begin{cases} M_{11} = \frac{I_y}{4} + \frac{1}{4}\left(\frac{c\theta_2}{2} + \frac{1}{2}\right)\left(\frac{I_x}{8} + \frac{9I_y}{4} - \frac{I_x c^2(2\theta_1)}{8} + \frac{I_y c^2(2\theta_1)}{4} - \frac{I_x c\theta_2}{8} + \frac{3I_y c(2\theta_1)}{2} + \frac{I_x c^2(2\theta_1)c\theta_2}{8}\right) \\ \quad +\ell^2 m\left(\left(\frac{c\theta_1}{\theta_1} - \frac{s\theta_1}{\theta_1^2} + \frac{s\theta_1(c\theta_2 - 1)}{\theta_2^2}\right)^2 + \left(\frac{(2c\theta_1 + \theta_1 s\theta_1 - 2)^2 + (\theta_1 - 2s\theta_1 + \theta_1 c\theta_1)^2}{\theta_1^2}\right)\right) \\ \quad +\ell^2 m\left(\frac{c\theta_1 - 1}{\theta_1^2} + \frac{s\theta_1}{\theta_1} - \frac{c\theta_1(c\theta_2 - 1)}{\theta_2^2}\right)^2, \\ M_{12} = \frac{I_x s(2\theta_1)s\theta_2}{16} + \frac{\ell^2 m(\theta_1 - s\theta_1)(2c\theta_2 + \theta_2 s\theta_2 - 2)}{\theta_1^2\theta_2^3}, \\ M_{21} = \frac{\ell^2 m(\theta_1 - s\theta_1)(2c\theta_2 + \theta_2 s\theta_2 - 2)}{\theta_1^2\theta_2^3} - \frac{I_x s(2\theta_1)s\theta_2}{16}, \\ M_{22} = \frac{I_x}{8} + \frac{\ell^2 m(2\theta_2^2 - 8\theta_2 s\theta_2 - 8c\theta_2 + 2\theta_2^2 c\theta_2 + 8)}{\theta_2^6}, \end{cases}$$

$$\begin{cases} C_{11} = -\frac{c\theta_1 s\theta_1\left(\frac{c\theta_2}{2} + \frac{1}{2}\right)\left(6I_y - I_x(2c^2\theta_1 - 1) + 2I_y(2c^2\theta_1 - 1) + I_x c\theta_2(2c^2\theta_1 - 1)\right)}{8} \\ \quad - \frac{\ell^2 m(48\theta_2^2 + 4\theta_1^4 + 16\theta_1^2\theta_2^2 + 2\theta_1^4\theta_2^2 - 48\theta_2^2 c\theta_1 - 4\theta_1^4 c\theta_1 - 4\theta_1^4 c\theta_2 - 2\theta_1^5 s\theta_1 - 48\theta_1\theta_2^2 s\theta_1)}{7\theta_1^7\theta_2^2} \\ \quad - \frac{\ell^2 m(8\theta_1^2\theta_2^2 c\theta_1 + 2\theta_1^4\theta_2^2 c\theta_1 + 4\theta_1^4 c\theta_1 c\theta_2 - 6\theta_1^3\theta_2^2 s\theta_1 + 2\theta_1^5 c\theta_2 s\theta_1)}{2\theta_1^7\theta_2^2}, \\ C_{12} = \frac{s\theta_2\left(9I_y - I_x c\theta_2 + 6I_y(2c^2\theta_1 - 1) + I_y(2c^2\theta_1 - 1)^2 + I_x c\theta_2(2c^2\theta_1 - 1)^2\right)}{32} \\ \quad + \frac{\ell^2 m(4c\theta_2 + 2\theta_2 s\theta_2 - 4)(\theta_1^2 + \theta_2^2 - \theta_1^2 c\theta_2 - \theta_2^2 c\theta_1)}{\theta_1^2\theta_2^5}, \\ C_{13} = \frac{I_x s(2\theta_1)c\theta_2}{16} - \frac{\ell^2 m(\theta_1 - s\theta_1)(6c\theta_2 + 4\theta_2 s\theta_2 - \theta_2^2 c\theta_2 - 6)}{\theta_1^2\theta_2^4}, \\ C_{21} = \frac{s\theta_2\left(9I_y + I_y c^2(2\theta_1) - I_x c\theta_2 + 6I_y c(2\theta_1) + I_x c^2(2\theta_1)c\theta_2\right)}{64} + \frac{I_x c(2\theta_1)s\theta_2}{8} \\ \quad - \frac{\ell^2 m(4c\theta_2 + 2\theta_2 s\theta_2 - 4)(\theta_1^2 + \theta_2^2 - \theta_1^2 c\theta_2 - \theta_2^2 c\theta_1)}{2\theta_1^2\theta_2^5} - \frac{\ell^2 m(\theta_1 - 2s\theta_1 + \theta_1 c\theta_1)(2c\theta_2 + \theta_2 s\theta_2 - 2)}{\theta_1^3\theta_2^3}, \\ C_{22} = 0, \\ C_{23} = \frac{I_x s(2\theta_1)c\theta_2}{16} - \frac{\ell^2 m(\theta_1 - s\theta_1)(6c\theta_2 + 4\theta_2 s\theta_2 - \theta_2^2 c\theta_2 - 6)}{\theta_1^2\theta_2^4}, \end{cases}$$

$$\begin{cases} K_1 = \frac{EI_b\theta_1}{\ell} + \ell g m\left(\frac{c\theta_1}{\theta_1} + \frac{2(c\theta_1 - 1)}{\theta_1^3} + \frac{s\theta_1(c\theta_2 - 1)}{\theta_2^2}\right), \\ K_2 = \frac{EI_b\theta_2}{\ell} - \ell g m\frac{c\theta_1(2c\theta_2 + \theta_2 s\theta_2 - 2)}{\theta_2^3}, \end{cases}$$

REFERENCES

[1] Russo M., Sadati S. M. H., Dong X., Mohammad A., Walker I. D., Bergeles C., Xu K., Axinte D.A. 203. Continuum Robots: An Overview, Adv. Intell. Syst. 5(5): 2200367.

[2] Honghong W., Mao Y., Du J. 2024. Continuum Robots and Magnetic Soft Robots: From Models to Interdisciplinary Challenges for Medical Applications, Micromachines. 15(3): 313.

[3] Kolachalama S., Lakshmanan S. 2020. Continuum Robots for Manipulation Applications: A Survey, J. Robot. 2020 (Article ID 4187048): 19.

[4] Gao G., Liu Y., Wang H., SongM. Ren H. 2015. Workspace Calculating and Kinematic Modelling of a Flexible Continuum Manipulator constructed by steel-wires, Industrial Robot. 42(6): 565-571.

[5] Gao G., Wang H., Liu J., Zheng Y. 2019. Statics Analysis of an Extensible Continuum Manipulator with Large Deflection, Mech. Mach. Theory. 141: 245-266.

[6] Amouri A., Zaatri A., Mahfoudi C. 2018. Dynamic Modeling of a Class of Continuum Manipulators in Fixed Orientation, J. Intell. Robot. Syst. 91(3-4): 413-424.

[7] Rone W. S., Ben-Tzvi P. 2014. Mechanics Modeling of Multi-Segment Rod-Driven Continuum Robots, J. Mech. Robot. 6(4): 041006.

[8] Amouri A., Cherfia A., Belkhiri A., Merabti H. 2023. Bio-Inspired a Novel Dual-Cross-Module Sections Cable-Driven Continuum Robot: Design, Kinematics Modeling and Workspace Analysis, J. Braz. Soc. Mech. Sci. Eng. 45: 265.

[9] Zhou P., Yao J., Zhang S., Wei C., Zhang H., Qi S. 2022. A Bioinspired Fish-Bone Continuum Robot with Rigid-Flexible-Soft Coupling Structure, Bioinspir. Biomim.

[10] Webster III, R. J., Jones B. A. 2010. Design and Kinematic Modeling of Constant Curvature Continuum Robots: A Review, Int. J. Robot. Res. 29(13): 1661-1683.

[11] Amouri A. 2019. Investigation of the Constant Curvature Kinematic Assumption of 2-DOFs Cable-Driven Continuum Robot, UPB Sci. Bull. D: Mech. Eng. 81(3): 27-38.

[12] Renda F., Boyer F., Dias J., Seneviratne L. 2018. Discrete Cosserat Approach for Multisection Soft Manipulator Dynamics, IEEE Trans. ROBOT. 34(6): 1518-1533.

[13] Djedili, A., Amouri, A., Laib dit Laksir, Y., Belkhiri, A. 2024. Performance Evaluation of Population-Based Metaheuristic Algorithms for Solving the Inverse Kinematic of a Class of Continuum Robots, UPB Sci. Bull. D: Mech. Eng.86(1): 33-46.

[14] Amouri A., Mahfoudi C., Zaatri A. 2015. Multiphysics modeling and simulation for systems design and monitoring, vol. 2, Contribution to Inverse Kinematic Modeling of a Planar Continuum Robot Using a Particle Swarm Optimization, Cham: Springer. pp. 141-150.

[15] Singh I., Lakhal O., Amara Y., Coelen V., Pathak P.M., Merzouki R. 2017. Performance Evaluation of Inverse Kinematic Models of a Compact Bionic Handling Assistant, in Proc. of IEEE International Conference on Robotics and Biomimetics (ROBIO), Macau, Macao. pp. 264-269.

[16] Hirose S. 1993. Biologically Inspired Robots, Oxford University Press, Oxford. pp. 147-155.

[17] Hirose S., Yamada H. 2009. Snake-like robots, IEEE Robot Autom Mag. 16(1): 88-98.

[18] Rone W. S., Ben-Tzvi P. 2014. Continuum Robot Dynamics Utilizing the Principle of Virtual Power, IEEE Trans. Robot. 30(1): 275-287.

[19] Bousbia L., Amouri A., Cherfia A. 2023. Dynamic Modeling of a 2-DoFs Cable-Driven Continuum Robot, World Journal of Engineering. 20(4): 631-640.

[20] Amouri A., Mahfoudi C., Zaatri A. 2021. Dynamic Modeling of a Spatial Cable-Driven Continuum Robot Using Euler-Lagrange Method, International Journal of Engineering and Technology Innovation. 10(1): 60-74.

[21] Janabi-Sharifi F., Jalali A., Walker I. D. 2021. Cosserat Rod-Based Dynamic Modeling of Tendon-Driven Continuum Robots: A Tutorial, IEEE Access. 9: 68703-68719.

[22] Till J., Aloi V., Rucker C. 2019. Real-Time Dynamics of Soft and Continuum Robots Based on Cosserat Rod Models, Int. J. Robot. Res. 38(6): 723-746.

[23] Belkhiri A., Amouri A., Cherfia A. 2023. Design of Fractional-Order PID Controller for Trajectory Tracking Control of Continuum Robots, FME Trans. 51(2): 243-252.

[24] Ghoul A., Kara K., Benrabah M. and Hadjili M. L. 2022. Optimized Nonlinear Sliding Mode Control of a Continuum Robot Manipulator, J. Control Autom. Electr. Syst. pp. 1-9.

[25] Amouri A., Cherfia A., Merabti H., Laib dit Laksir Y. 2022. Nonlinear Model Predictive Control of a Class

of Continuum Robots Using Kinematic and Dynamic Models, FME Trans. 50(2): 339-350.

[26] Amouri A., Merabti H., Cherfia A., Laib dit Laksir Y. 2022. Nonlinear Model Predictive Control for Trajectory Tracking of a Class of Continuum Robots, UPB Sci. Bull. D: Mech. Eng. 84(3): 19-32.

[27] Peng J., Xu W., Yang T., Hu Z., Liang B. 2020. Dynamic Modeling and Trajectory Tracking Control Method of Segmented Linkage Cable-Driven Hyperredundant Robot. Nonlinear Dynamics. 101(1): 233-253.

[28] Haotian B., Lee B. G., Yang G., Shen W., Qian S., Zhang H., Zhou J., Fang Z., Zheng T., Yang S., *et al*. 2024. Unlocking the Potential of Cable-Driven Continuum Robots: A Comprehensive Review and Future Directions, Actuators. 13(2): 52.

[29] Zhang J., Kan Z., Li Y., Wu Z., Wu J., Peng H. 2022. Novel Design of a Cable-Driven Continuum Robot with Multiple Motion Patterns, IEEE Robot. Autom. Lett. 7(3): 6163-6170.

[30] Dehghani M., Moosavian S. A. A. 2014. Dynamics Modeling of a Continuum Robotic Arm with a Contact Point in Planar Grasp, J. Robot. 2014(Article ID 308283): 13.

[31] El-Hussieny H., Hameed I. A., Ryu J. H. 2020. Nonlinear Model Predictive Growth Control of a Class of Plant-Inspired Soft Growing Robots, IEEE Access. 8: 214495-214503.

[32] Podlubny I. 1999. Fractional-Order Systems and PI/sup /spl lambda//D/sup /spl mu//-Controllers, IEEE Trans. Autom. Control. 44(1): 208-214.

[33] Kennedy J., Eberhart R. 1995. Particle Swarm Optimization, in Proc. of International Conference on Neural Networks, WA, Australia. 4: 1942-1948.